Geophysical and Geochemical Constraints on Deep Weathering and Water Storage Potential in the Southern Sierra Critical Zone Observatory

W. Steven Holbrook[1], Clifford S. Riebe[1], Jorden Hayes[1], Dennis Harry[2], Kyle Reeder[2], Armen Malazian[3], Anthony Dosseto[4], Barbara Jessup[1], Peter Hartsough[3], and Jan Hopmans[3]

[1] Department of Geology and Geophysics, University of Wyoming, Laramie, WY 82071

[2] Department of Geosciences, Warner College of Natural Resources, Colorado State University, Ft Collins, CO 80523

[3] Department of Land, Air and Water Resources, University of California, Davis, CA 95616

[4] School of Earth and Environmental Science, University of Wollongong, Australia

Abstract

Quantifying the depth and degree of subsurface weathering in landscapes is crucial for quantitative understanding of the biogeochemistry of weathering, the mechanics of hillslope sediment transport, and biogeochemical cycling of nutrients and carbon over both short and long timescales. Although the degree of weathering has often been measured from geochemical and physical properties of regolith and rock, quantifying the thickness of subsurface weathering has remained challenging, in part because the interface between altered and unaltered rock is often buried at difficult to access depths. To overcome this challenge, we used seismic refraction and resistivity surveys to estimate regolith thickness and generate representative images of subsurface weathering and water storage at the Southern Sierra Critical Zone Observatory (SSCZO). Inferred seismic velocities and electrical resistivities of the subsurface provide evidence for a surprisingly thick weathering zone, with unweathered granite lying an average of 25 m below the surface, and highly weathered saprolite extending to an average depth of 10 m. Our cosmogenic nuclide based estimates of erosion rates vary from XX to XX m/Ma across the site; hence measured regolith thicknesses correspond to a turnover times of XX,000 and XX,

1

0000 years for the profile as a whole and for highly weathered saprolite, respectively, indicating that weathering measured from regolith at the surface integrates subsurface weathering over late Pleistocene variations in climate. Hence, to the extent that climate modulates subsurface weathering at the SSCZO, modern surface processes may be influenced to a legacy of past conditions. Porosities derived from a rock physics model of seismic velocities decrease from XX % to zero at the base of weathered rock along one intensively studied transect. Model-predicted porosities are broadly consistent with values measured from both physical and chemical properties of saprolite and rock, suggesting that our analysis of the geophysical data provides robust first-order constraints on subsurface weathering and water storage across the SSCZO. Our results indicate that saprolite is both a crucial reservoir of water and major source of weathering fluxes, accommodating an average of XX m^3/m^2 of water and accounting for roughly XX% of the total chemical erosion flux at the SSCZO.

Introduction

Weathering at the interface between bedrock and regolith represents the inception of surface processes, breaking rock down by physical disaggregation (e.g., Wahrhaftig, 1965; Roering et al., 2010) and chemical alteration (e.g., Ruxton and Berry, 1958; Buss et al., 2008), and thus initiating its journey through the critical zone. As erosion at the surface exhumes minerals through saprolite, continued subsurface weathering influences regolith resistance to both soil production (e.g., Dixon et al., 2009) and downslope transport at the surface (Yoo et al., 2009), thus indirectly regulating geomorphic processes that generate relief at hillslope to mountain scales (Ruxton and Berry, 1958; Wahrhaftig, 1965; Dixon et al., 2009; Jessup et al., 2011). Moreover, by altering minerals (White et al., 1998) and disrupting regolith along both mineral

grain boundaries (Wahrhaftig, 1965) and preexisting joints and fractures (CITE), subsurface weathering also generates porosity (Sitchler et al., YEAR) and liberates nutrients (CITE), making it a crucial regulator of both water storage potential (Graham et al., 2010) and nutrient cycling (CITE) in landscapes. Over millions of years, solute fluxes from the deep subsurface contribute to silicate weathering's influence on atmospheric CO_2 (Calmels et al., 2011; Derry et al., 2011???), thus affecting global climate through the greenhouse effect (Walker et al., 1981). Hence, a quantitative understanding of subsurface weathering is important across a remarkably broad range of problems in critical zone research, involving the biogeochemistry of weathering, the mechanics of hillslope sediment transport, and the biogeochemical cycling of nutrients and carbon over both short and long timescales.

Subsurface weathering also reflects as well as regulates critical zone processes. For example, both the thickness and degree of depletion in regolith shed light on the balance between weathering which breaks rock down, and erosion which carries it away and thus regulates residence time near the surface for minerals (Ferrier and Kirchner, 2008). If weathering is intense and near-surface residence times are long (Ferrier and Kirchner, 2008; Gabet and Mudd, 2009; Hilley et al., 2011), regolith may be thick and highly weathered (Graham et al., 2010 -- OR OTHER Graham reference; Dethier and Lazarus, 2006). Conversely, if weathering is inhibited and residence times are short (Ferrier and Kirchner, 2008; Norton and von Blanckenburg, 2010), regolith may be thin and weakly weathered (Anderson et al., 2002; Roering et al., 2010). Thus, quantifying the thickness and degree of weathering in regolith constrains the relative importance of weathering and erosion (Waldbauer and Chamberlain, 2005; Ferrier and Kirchner, 2008; Hilley et al., 2011) and also reveals how the balance between

chemical and physical erosion varies with factors such as climate (Riebe et al., 2004a,b; Dixon et al., 2009) and tectonics (Riebe et al., 2004a).

Although the degree of weathering can generally be measured straightforwardly from geochemical (Nesbitt 1979; Parker etc. CITE) and physical (CITE) properties of samples collected from a landscape, quantifying the thickness of weathering has remained challenging, in part because the interface between altered and unaltered rock is often buried at difficult to access depths. Lack of access to the bedrock-regolith interface has also impeded understanding of mechanisms that influence rates of regolith production from rock (Fletcher CITE), which in turn ultimately limit the pace of erosion and landscape evolution. For example, it has been proposed that regolith production rates should be faster under thinner regolith (Hren et al., 2007; Hilley and Porder, 2008; Hilley et al., 2011), because thinner regolith promotes tighter coupling with surface-based weathering mechanisms such as throughflowing meteoric water and root-related disruption of the bedrock-regolith interface (Roering et al., 2010). Hence, in theory, regolith production rates may decrease with regolith thickness (Hren et al., 2007; Hilley and Porder, 2008; Hilley et al., 2011) in much the same way that soil production rates have been observed to decrease with soil thickness (Heimsath et al., 1997; 2001). However, in practice, the regolith production function has been difficult to quantify (Dossetto et al., 2008; Brantley et al., 2011), in part because of difficulties in coupling regolith production rates with representative measurements of regolith thickness.

Drilling provides direct, point measurements of regolith thickness, but is prone to unrepresentative sampling when the depth of weathering varies. Hence, many boreholes may be needed for a representative distribution of thicknesses (Dethier and Lazarus, 2006), making drilling a potentially costly or misleading method for measuring depth of weathering in

landscapes. Moreover, drilling alone may not reveal any progressive changes in degree of weathering with depth, such as multiple weathering fronts (cite Brantley et al., YEAR) or gradients in porosity with depth. Downhole logging and sample collection by coring may overcome this limitation, but can be costly and, like drilling, are prone to unrepresentative sampling of just a few, potentially anomalous points on the landscape. Geophysics, in contrast, can be inexpensively applied over broad scales to quantify a variety of subsurface properties that relate to weathering. For example, P-wave velocities in the shallow subsurface (Befus et al., 2011) are influenced by porosity and density (CITE), and thus may reflect progressive changes in weathering with depth and also major subsurface boundaries, including the bedrock-regolith interface. Resistivity, on the other hand, is influenced by subsurface concentrations of water and clay, which reflect mass loss and degree of alteration due to subsurface weathering. Despite the outstanding potential of these and other geophysical measurements as tools for characterizing otherwise difficult-to-access regolith, they have not been widely used in studies of subsurface weathering.

Here we present results of geophysical investigations of subsurface weathering in the Southern Sierra Critical Zone Observatory (SSCZO), where we are able to leverage ongoing geochemical and isotopic studies of regolith and rock (Dixon et al., 2009; Jessup et al., 2011) for a unique, multifaceted perspective on landscape weathering and erosion. Using seismic velocity and electrical resistivity data, we show evidence for a surprisingly thick weathering zone; in virtually all surveys conducted in the area, our data suggest that unweathered granite lies an average of 25 m below the surface. Moreover, the thickness of highly weathered saprolite is roughly 10 m on average, based on observed thicknesses of regolith with P-wave velocities <2 km/s. Our cosmogenic nuclide based estimates of erosion rates vary from XX to XX m/Ma

across the site; hence measured regolith thicknesses correspond to a turnover times of XX,000 and XX,0000 years for the profile as a whole and for highly weathered saprolite, respectively, indicating that weathering measured from regolith at the surface integrates subsurface weathering over late Pleistocene variations in climate. To the extent that these variations in climate have modulated subsurface weathering across the SSCZO, modern surface processes in the landscape may be influenced by a legacy of past conditions. Porosities derived from a rock physics model of seismic velocities are as high as XX%, decreasing with depth (where velocities are higher) and assumed clay content in the model. Model-predicted porosities are broadly consistent with those measured from both physical and chemical properties of saprolite and rock. This suggests that our analysis of the geophysical data provides robust first-order constraints on subsurface weathering and water storage across the SSCZO. Together our results indicate that saprolite is both a crucial reservoir of water and major source of weathering fluxes, accommodating an average of XX m^3/m^2 of water on one closely investigated slope and accounting for roughly XX% of the total chemical erosion flux at the SSCZO.

Setting

The Southern Sierra CZO is located in Fresno County, California, USA, near the divide between the San Joaquin and Kings rivers. The area is underlain by granitic bedrock, outside the limits of recent glaciation. It lies in the heart of the so called "stepped topography" (Wahrhaftig, 1965; Jessup et al., 2011), a sequence of range-parallel ridges and valleys, with alternating steep and gentle terrain. The steep "steps" and gentle "treads" are thought to arise from differences in weathering susceptibility of bare versus soil-mantled rock, with steps being a locus of bare rock and slow erosion and treads being a locus of soil cover and fast erosion (Wahrhaftig, 1965). Roadcuts in the area typically expose a simple sequence of saprolite (i.e., chemically weathered

6

but physically intact rock) overlying fresh granite, suggesting that variations in geophysical properties of the subsurface may often be straightforwardly interpreted to reflect variations in porosity and secondary mineral abundance.

The CZO lies within the Kings River Experimental Watershed (KREW), a site of long-term research by the Pacific Southwest Research Station of the US Forest Service (Hunsaker and Eagan, 2003). Three of the four CZO catchments, called P301, P303 and P304 (Fig. 1a), with areas of 0.99, 1.32, and 0.49 km^2, respectively, are drained by Providence Creek, which ultimately joins Big Creek, a tributary of the Kings River. The other CZO catchment, called D102, drains the uppermost 1.21 km^2 of the Duff Creek catchment, immediately south of Providence Creek.

Vegetative cover, where present, is dominated by a mixed-conifer forest, consisting of white fir (*Abies concolor*), ponderosa pine (*Pinus ponderosa*), Jeffrey pine (*Pinus jeffreyi*), black oak (*Quercus kelloggii*), sugar pine (*Pinus lambertiana*), and incense cedar (*Calocedrus decurrens*), with minor cover by mixed chaparral. Soils in the catchments have been described as coarse-loamy, mixed, superactive, humic Dystroxerepts of both the mesic and frigid varieties (Giger and Schmitt, 1993). Soils in the catchments have an average thickness (i.e., depth to saprolite) of 65±5 cm and an average bulk density of 1.38±0.09 g cm^{-3} (Johnson et al., 2011). Mean annual precipitation is approximately 110 cm yr^{-1} and mean annual temperature is approximately 9 °C. The style of precipitation varies from dominantly snow-derived at the heads of the catchments to dominantly rain-derived at the catchment mouths.

An improved understanding of the water balance at catchment scales is a major research goal of the SSCZO (Bales et al., 2011). Of particular interest are data and analyses that inform partitioning of deep and shallow water fluxes in the subsurface. Another goal is to explore implications of subsurface water flow and storage for the ecosystem, including questions of

where vegetation gets water and how this changes throughout the year (CITE). Observations of soil moisture, snow pack, and sap flow from a heavily instrumented white fir tree (CZT-1) show that roughly one third of its annual evapotranspiration is derived from depths > 1 m (Bales et al., 2011), suggesting that water storage and through-flow in the deep subsurface may be a major component of the overall water budget for the ecosystem. We use our geophysical measurements, described next, to test this hypothesis at the hillslope scale along our transects.

Acquisition and Processing of Data and Samples

Geophysical Survey Design

To obtain a representative picture of subsurface weathering at the SSCZO, we acquired geophysical data on seven transects spanning a mix of N-S and E-W trending ridges and meadows in the CZO (Fig. 1). Our survey design enables provisional tests for strong aspect-driven trends in CZ architecture, such as those observed by Befus et al. (2011) on crystalline slopes in the Boulder Creek CZO. It also allows us to explore the hydrologic coupling of hillslopes and meadows.

Six of the seven surveys reported here are underlain by Dinkey Creek granodiorite (Bateman and Wones, 1972), a fairly uniform, medium-grained hornblende-biotite granodiorite, with abundant disc-shaped mafic inclusions. The seventh (Line 9) was situated on a bare expanse of Bald Mountain Quartz Monzonite (Bateman and Wones, 1972), which is also medium grained, but devoid of hornblende and mafic inclusions. Topography on all lines was surveyed using a tape measure and inclinometer. Five lines span soil-mantled slopes in P301 (Lines 3-7; Fig. 1B, and E), one spans a convex soil-mantled ridge in D102 (Line 2; Fig. 1D), and

the last spans bare rock in Glen Meadow (Line 9; Fig. 1C), examined here for reference in identifying the base of weathered regolith in the other transects.

Seismic Refraction Surveys and Tomographic Inversions

On each of the surveyed lines, we acquired seismic refraction data using two 24-channel Geometrics Geode systems and 40 Hz vertical-component geophones, with a 12-pound sledgehammer source striking a ~20 x 20 x 2 cm-thick stainless steel plate. In some instances we supplemented data acquisition with 12-gauge shotgun blanks fired from a buffalo gun with muzzle implanted 1-2 meters deep in 2 inch-diameter auger holes. Geophone spacing varied from XX m (Lines XX, XX) to 5 m (Lines XX and XX). On Line 9, 24 geophones at XX m spacing were attached to the outcrop using plaster of paris, and sledgehammer blows were landed directly on the outcrop. Shot spacing varied from 5 m (Line 2 CHECK) to 10 m (all other lines).

We produced seismic velocity models using first-arrival, travel-time tomography. First arrival times were picked manually on all traces with sufficient signal-to-noise ratios (e.g., Figure 2). Travel times were inverted for each line using SeisImager$^©$ software as follows. First, an initial velocity model was generated by inserting a uniform vertical velocity gradient (usually from 300 m/s to 4500 m/s) beneath the elevation profile on the line. For the tomographic inversion, the model is discretized into cells of constant velocity; cell size in our models was XXXXX. [Something about discretization… layer thickness… etc.] [Something about raytracing method… looks like shortest path, but must verify…] Ten iterations of a linearized least-squares inversion algorithm were conducted. No smoothing was applied during the inversion. Typical agreement between predicted and observed travel times is shown in Figure 3; agreement is generally lower for longer travel times, which reflect information from

the deepest parts of the profile, where ray coverage is lowest and thus provides least constraints on the inversion. Here the deepest coverage by ray paths is ~30-50 m, dictated mostly by the overall length of the geophone array in each survey .

In a linearized inversion, the final result can be highly dependent on the starting model. The starting model must be relatively "good" in order for the inversion to converge to a reasonable solution. Moreover, the final result will often carry vestiges of the starting model. For example, a starting model that consists of a simple linear increase in velocity with depth will generally produce a smoother final model than a layered starting model, which will often lead to a final model that retains sharp velocity increases where the original velocity steps were. Hence, we argue that our use a simple linear increase velocity for our starting models is justified in the absence of a priori knowledge of the positions of any sharp transitions in velocity with depth.

Our tomographic inversion of seismic refraction data from Line 5 yields the velocity model shown in Figure 4. To quantify representative uncertainties for our velocity models -- in particular, the dependence on starting velocity model -- we conducted a Monte Carlo error analysis on Line 5. This involved 50 independent inversions from a suite of starting velocity models wherein velocity increases linearly with depth from 0 to 50 m (Figure 5). Velocities at the surface and at 50 m depth were varied from 300 to 700 m/s, and from 3000 to 5300 m/s, respectively, resulting in a total velocity variation among starting models of about 800 m/s at 10 m depth, 1000 m/s at 20 m depth, and 1500 m/s at 30 m depth (Figure 5). Velocity inversion parameters were held constant for all runs. The distribution of variance in modeled velocities is shown both in percent error and standard deviation in Figure 5. Percent errors are typically ~5-10%, with velocities in the upper 10 m being known to within 100 m/s or less, and

uncertainties of ±300 m/s or more elsewhere. Hence our Monte Carlo analysis suggests that our tomographic inversion of Line 5 is not highly sensitive to variations in starting model.

Velocity models for all of the other lines are shown in Figure 6. Line 9 (Figure 6) is unique in that it offers an opportunity to identify the velocity that corresponds to relatively unweathered rock exposed on an extensive outcrop. The data on Line 9 are unlike any of the data acquired on ridge or meadow lines, in two important ways. First, at small source-receiver offsets, the first arrivals have nearly linear slopes that indicate velocities of ~4.0 km/s at the surface (dashed line, Fig. 2, Line 9). Second, the first arrivals have a high frequency content, with a center frequency around 400 Hz. In contrast, all other lines have much slower first-arrival velocities and a lower frequency content, with a typical center frequency around 50 Hz. These characteristics are consistent with a subsurface consisting of relatively unweathered bedrock with a nearly constant velocity of 4.0 km/s and low degrees of attenuation (Fig. 6). This observation enables us to confidently interpret velocities of 4.0 km/s, where encountered in the subsurface of other lines, as unweathered bedrock.

Electrical Resistivity Measurements and Modeling

Because they are sensitive to electrical conductivity (or, equivalently, resistivity) rather than elastic properties (e.g., velocity), electrical data provide an important complement to seismic refraction data. In particular, resistivity values can help distinguish between two possible causes for increased seismic velocity: decreasing porosity (i.e., less weathering) or increasing saturation of the pore space (i.e., the water table).

Hence, for Line 5 we also acquired resistivity data using a 48-channel IRIS Instruments, Inc., Syscal Pro 48©. To cover the entire transect, we spaced stainless steel electrodes on the

ground at 10 m intervals to create a 470-m-long line and used a dipole-dipole array with fixed

10 m spacing between the current and voltage electrodes. During data acquisition we varied the

distance between the current and voltage electrode pairs from 1 to 10 times the electrode

spacing (i.e., 10-100 m) using current supplied by a 12-volt battery.

Data from Line 5 were edited to remove outliers with negative voltage drops or apparent

resistivity greater than 20,000 ohm-m. This reduced the dataset by approximately six percent. A

two dimensional subsurface resistivity model was generated using DCPIP2D [Oldenburg and

Li, 1994]. The inversion is regularized by applying weighing parameters α_s, α_x, and α_z, which

control the relative importance of the starting model and the horizontal and vertical

smoothness, respectively, in the determining the solution. Subsurface resistivity was modeled

along the line of the profile on a 108x32 mesh. Horizontal cell dimensions were 5 m (half the

electrode spacing) within the area encompassed by the electrode array. Wider cells (10 m width

increasing to 160 m) were used to extend the mesh 320 m beyond either end of the array. Vertical

cell dimensions were 2.5 m for the first 32.5 m depth, with cell thickness increasing downward

to extend the model to 450 m depth (close to the array length). A series of models were

examined to test the effects of a finer mesh size, the initial model used to begin the inversion

process, and the weighting factors αs, αx, and αz. All models tested produced similar

subsurface resistivity models within the upper 100 m in the region encompassed by the array,

achieving a global variance between the modeled and observed voltages of less than 3mV. The

preferred model uses $\alpha_s = 0.001$, $\alpha_x = 3$, and $\alpha_z = 1$.

Modeled apparent resistivity pseudosections show a good fit with observed resistivities

throughout most of the profile (Figure 7), indicating that the inverse model achieves a good

global fit (as measured by the variance) and also fits well for all combinations of current and

potential electrode pairs. The exception is the lower left portion of the pseudosection (corresponding to widely spaced current-potential electrode pairs near the left end of the line). In this region, the modeled apparent resistivity structure is somewhat smoother than observed. This may be caused by complexity in the deeper subsurface near the left end of the array, or it may be caused by weaker signal at large electrode offsets in this area.

The preferred inverse model shows strong contrasts in electrical properties along Line 5 that correlate well with observations of the substrate at the surface (Fig. 8). Resistivity ranges from 10^1-10^5 ohm-m (Fig. 8) and is generally higher (> 10^4 ohm-m) beneath the hill on the south side of the profile than beneath the swampy meadow to the north (10^1-10^4 ohm-m). The boundary between the high and low resistivity regions is sharp, marked by a steep resistivity gradient. Material with low resistivity is relatively thin (10 m thick or less) on the hillslope and thickens abruptly to > 70 m near the base of the hill. The low resistivity extends to > 70 m depth beneath the meadow, with very low values (a few hundred ohm-m) occurring in the upper 20 m beneath the center of the valley floor.

To assess which portions of the model are robust (that is, well-resolved by the data) we calculated the Depth of Investigation (DOI) Index [Oldenburg and Li, 1999]. To calculate the DOI Index, two inversions are run with very different reference models (in this case, 100 ohm-m and 10,000 ohm-m). The model weights are chosen to cause the model to revert to the reference model resistivity in areas poorly constrained by the data. In these areas, the two inverse models will differ by the difference in their starting models. Areas where the two models are similar correspond to regions of the model that are well constrained by the data. The DOI Index is a normalized measure of the similarity of the two models, with a DOI Index of 0 representing perfect similarity and a DOI Index of 1 indicating areas where each model has reverted to its

reference model. Empirical evidence suggests a DOI Index less than 0.1-0.2 may be considered robust. For the preferred model, the DOI Index indicates that the upper 70-100 m of the model is robust. In particular, high resistivity (> 10^4 ohm-m) extending to great depth beneath the hill, the abrupt change from high to low resistivity (<10^4 ohm-m) in the subsurface beneath the hillside, and very low resistivity (<10^3 ohm-m) extending to great depth beneath the valley are well resolved features in the model.

Bulk Density and Porosity

To put additional constraints on variations in subsurface weathering across the site, we measured saprolite porosity (Φ), i.e., its volumetric water-storage capacity, using Equation 1.

$$\Phi = 1 - \rho_W \Big/ \rho_S$$

Eq. 1

Here, ρ_W is bulk density, measured from volumetric samples of weathered regolith, and ρ_S is the particle density, here assumed to be 2.65 g cm^{-3} (Flint and Flint, 2002).

To quantify ρ_W and how it varies both laterally and with depth, we collected samples from depths of 25 to 540 cm by augering into saprolite at five locations within a 5 m radius of CZT-1, located near the crest of the ridge spanned by Line 5 (Fig. 1B and Table 1). We also augered into the subsurface at two additional points along Line 5 to collect samples for comparison with geophysics-based estimates of subsurface porosity (as discussed in a later section). All samples were collected coincident with the geophysical surveys, in September and October, 2011. At each point, we first hand augered a hole to just above the target sampling depth, and then drove a cylinder of known volume into the underlying saprolite using a slide-hammer attachment on either a Madera© sampler (for shallow depths) or an AMS© sampler (for

deeper depths). To minimize compaction that might be induced by the hammer, we used marks

on the sampler as a gauge on when to stop driving the cylinder.

We measured the mass of each sample in both the field and laboratory before oven

drying them for 24 hours at 105 °C (Flint and Flint, 2002). We massed the samples again after

allowing samples to cool (thus minimizing effects of convection) for estimates of dry soil mass,

which in turn enables calculation of bulk density (based on the known cylinder volume), used

here in Equation 1 to estimate porosity.

Results for our porosity measurements are shown in Table 1. Porosity ranges from 0.36

to 0.52, with higher values generally near the surface.

Chemical Depletion Fractions

To quantify the intensity of chemical weathering at our sites, we calculate chemical

depletion fractions (*CDFs*) using measurements of bulk chemistry from widely distributed

samples of soil, saprolite, and bedrock. *CDF* expresses the fraction of the overall denudation

rate (*D*) that is accounted for by chemical erosion (*W*) (Riebe et al., 2001a; Riebe et al., 2003), as

shown in Equation 2.

$$CDF = W\!/\!D = 1 - Zr_P\!/\!Zr_W$$

Eq. 2

Here, Zr_P and Zr_W are the concentrations of an immobile element (in this case zirconium) in

unweathered parent bedrock and weathered daughter material, respectively. Equation 2 arises

from a steady-state geochemical mass balance, wherein the rock-to-regolith enrichment of

immobile elements is a reflection of depletion of relatively soluble components of the regolith

(Stallard 1985; Riebe et al., 2001a; 2003). For saprolite, where all mass losses are chemical by

definition (Anderson et al., 2002; Riebe et al., 2003; Dixon et al., 2009), the right side of Equation 2 is equivalent to the sum of all of the mass transfer coefficients (τ_X) for the individual elements (denoted by X) (Brimhall and Dietrich, 1987), except in algebraic sign (i.e., $CDF = -\sum \tau_X$). Assuming that weathering of saprolite is isovolumetric (i.e., such that strain = 0), the mass loss due to weathering corresponds directly to changes in density and thus porosity (i.e., such that $CDF = \Phi$).

To measure $CDFs$, and thus estimate Φ independently of Equation 1 (i.e., using bulk geochemistry instead of density), we subsampled saprolite from the same auger holes of our bulk density analysis for bulk geochemical analysis using X-ray fluorescence (XRF). Using standard techniques (CITE) we created pressed pellets from mechanically powdered splits of our samples (Riebe 2000) for analysis on a 4 kW PANalytical AXIOS wavelength-dispersive XRF spectrometer. We reference the resulting measurements of Zr in saprolite (Zr_W) to a previously published average value of Zr in CZO bedrock (Riebe and Granger, this volume), in our calculation of $CDFs$ from Equation 2.

Results are shown in Table 2. $CDFs$ range from XX to XX.

Landscape-Scale Denudation Rates

Our geophysical and geochemical measurements provide a snapshot of the thickness and degree of weathering in the Southern Sierra CZO. To put these measurements into a temporal context, we collected sediment from the outlets of P301, P303, P304 and D102 (Fig. 1) and measured in-situ produced cosmogenic [10]Be in the quartz fraction of our samples, thus constraining near-surface residence times for sediment in the catchments (Lal and Arnold, 1985); relatively high [10]Be concentrations reflect relatively long near-surface residence times

because [10]Be production declines rapidly with depth below the surface. Assuming that erosion has been roughly steady over the timescale of nuclide accumulation, and that stream sediment is well mixed, we can use our [10]Be measurements in Equation 3 to infer spatially averaged denudation rates (D, in M L^{-2} T^{-1}) for the slopes upstream of our sampling sites (e.g., Brown et al., 1995; Bierman and Steig, 1996; Granger et al., 1996).

$$N = \frac{1}{D}\left(P_n\Lambda_n + P_{m1}\Lambda_{m1} + P_{m2}\Lambda_{m2} + P_{m3}\Lambda_{m3}\right)$$
　　　　　　　　　　　　　　　　　　　　　　　　　　　　　Eq. 3

Here N is the concentration of cosmogenic [10]Be in quartz, and P and Λ are the rate and penetration scaling factor of production of [10]Be in regolith, with subscripts denoting production by neutron spallation (n), muon capture ($m1$ and $m2$), and fast muon reactions ($m3$) (after Granger and Riebe, in review). Equation 3 is the solution to a differential equation that expresses the buildup of [10]Be in minerals during steady erosion to the surface through rock and regolith. It approximates the relationship between nuclide production rates and depth with a series of exponential functions (Granger and Smith, 2000) and assumes that the radioactive meanlife of [10]Be (τ_{Be-10}) is long compared to the erosional timescale (equal to Λ/D). The latter should be reasonable in this case, given that τ_{Be-10} = 2.00±0.02 Ma (Chmeleff et al., 2010) and Λ_n/D is ~0.01 Ma for denudation rates typical of granitic terrain elsewhere in the Sierra Nevada (e.g., Riebe et al., 2000). A corollary worth noting is that cosmogenic nuclides average erosion over millennial timescales, and thus are not strongly influenced by effects of recent land use, but rather tend to reflect background average rates of surface processes.

Although formulations similar to Equation 3 are widely used to infer landscape-scale erosion rates from cosmogenic nuclides (Balco et al., 2008), they can lead to substantial errors if chemical erosion accounts for a significant fraction of the overall landscape denudation (Riebe

and Granger, this issue; Dixon et al., 2009). To correct for the effects of chemical erosion, we multiply each of the production rate terms in parentheses in Equation 3 by an appropriate chemical erosion factor (*CEF$_i$*), e.g., as expressed in Equation 4 (after Riebe and Granger, this volume).

$$CEF_i = \frac{Zr_{sap}}{Zr_P}\left[\frac{Zr_{soil}}{Zr_{sap}}\left(1 - e^{-\rho h/\Lambda_i}\right) + e^{-\rho h/\Lambda_i}\right] \qquad \text{Eq. 4}$$

Here, Zr_{sap} and Zr_{soil} are the concentrations of zirconium in saprolite and soil, respectively, ρ and h are soil density and thickness, and Λ_i is the corresponding penetration scaling factor for the production term in question. In using Equation 4, we assume that Zr enrichment is a suitable proxy for quartz enrichment; this should be reasonable given that they are both highly resistant to chemical weathering (Riebe et al., 2001b).

To solve Equation 3 for the average denudation rate of each catchment, we need to estimate site-specific values of P and Λ for each nuclide production mechanism. We did so using published production rates and scaling factors that account for differences in altitude, latitude, and topographic shielding, which all influence the ambient flux of cosmic radiation and thus modulate production rates both at the surface and at depth (Lal, 1991; Dunne et al YEAR; Balco et al., 2008). Values used here are reported in Table 2. To quantify representative *CEFs* for each production rate term (Equation 4), we used average Zr concentrations in rock, saprolite, and soil, compiled for the SSCZO by Riebe and Granger (this volume), together with average soil depth (65±5 cm) and bulk density (1.38±0.09 g cm^{-3}) based on data from a site-spanning network of 53 quantitative soil pits (Johnson et al., 2011).

To measure ^{10}Be concentrations in quartz (i.e., *N* in Equation 3), we used standard techniques to first isolate and purify quartz from our sediment samples (e.g., Kohl and Niishizumi, 1992). We then dissolved the quartz in a 5:1 HF/HNO$_3$ solution after adding a ~3.5 x 10^{-4} g spike of ^{9}Be (with ^{10}Be/^{9}Be ratio = 9±2 x 10^{-15}) to each sample. Next, we fumed the dissolved quartz at 325°C in trace-metal-grade H$_2$SO$_4$ (to break apart fluoride complexes) and extracted and purified the Be using pH adjustment and preparative ion-exchange chromatography. Isolates of Be(OH)$_2$ were converted to BeO, mixed with Nb, and packed into stainless steel targets, which were sent to Purdue Rare Isotope Measurement (PRIME) Lab for analysis by Accelerator Mass Spectrometry (AMS) (Musikar et al., 2003). AMS analyses yield ^{10}Be/^{9}Be ratios, which we adjust using measured ^{10}Be/^{9}Be ratios in process blanks, and then convert to ^{10}Be concentrations using measured initial masses of quartz and ^{9}Be in added spikes. We then use our ^{10}Be concentrations, along with our estimates of *CEFs* and production rates, to estimate spatially averaged erosion rates for the CZO catchments from Equation 3.

Results are shown in Table 3. ^{10}Be concentrations range from XX to XX. Catchment averaged denudation rates range from XX to XX.

Discussion

Porosity model

Velocity in saprolite is lower than that of unweathered granite for two main reasons: increased porosity due to weathering, and the replacement of minerals such as feldspars with lower-velocity clays (weathering REF). We can estimate the porosity distribution in the subsurface from our seismic velocity models by predicting the velocity of a mineral aggregate over a range of possible porosities and finding the porosities that provide the best match to the observed velocities. We predict seismic velocity as a function of porosity and mineralogy with a

rock physics model based on Hertz-Mindlin contact theory [*Mindlin*, 1949], as formulated by *Helgerud et al.* [1999]. This approach treats rocks as aggregates of randomly packed spherical grains and expresses their bulk elastic properties (bulk modulus, K, and shear modulus, G) as functions of effective pressure, porosity, the elastic properties of constituent minerals, and a critical porosity (ϕ_c), which is the porosity above which the aggregate transitions from a suspension to a grain-supported material (typically 36-40%; [*Nur et al.*, 1998]). We assume a ϕ_c of 0.38 and use the modified upper and lower Hashin-Shtrikman bounds [*Dvorkin and Nur*, 1996], respectively, to calculate elastic moduli above and below ϕ_c. Given that most of the shallow subsurface is in the vadose zone, and therefore unsaturated, we model dry porosity; this provides a minimum estimate of porosity, since saturated rocks have higher velocities than dry rocks and thus a higher potential porosity than dry rocks of equal velocity. We tested the sensitivity of our predicted velocities (and thus porosities) to composition by modeling the elastic properties of the solid frame over a range of 25-50% quartz (K=44 GPa, G=36.6), 10-65% feldspar (K=70 GPa, G=30 GPa), and 0-65% clay (K=20.9 GPa, G=6.85 GPa), which will simulate the effects of a large range of degree of weathering of feldspars to clays (elastic constants from *Helgerud et al.* [1999] and REF). These minerals are typically the dominant minerals in a granite weathering zone (e.g., [*Ceryan*, 2008]); variations in minor secondary minerals will not significantly affect the predicted velocities. Bulk solid elastic constants were calculated using the averaging formula of *Hill* [1952]. Once the bulk and shear moduli of the medium for a given porosity are calculated, P-wave velocity can be calculated from

$$V_p = \sqrt{\frac{K + \frac{4}{3}G}{\rho_b}}$$

Eq. 5

where ρ_b is bulk density, calculated from $\rho_b = \phi\rho_w + (1 - \phi)\rho_{solid}$, where ρ_w is the density of water and ρ_{solid} the average density of the solid mineral constituents. We then compare the predicted velocities over our range of porosity values to the observed velocity to find the best-fitting porosity at each grid point in the velocity model.

A porosity model calculated in this way, assuming a mineralogy of 50% feldspar, 25% quartz, and 25% clay, shows that substantial porosity exists in the saprolite beneath much the surface on Line 5 (Figure 9). Predicted porosities are about 0.4±0.1 at the surface, decreasing with depth to zero at around 25-30 m depth (shallower in places). On average beneath the hillslope, porosity is 0.2 or higher in the upper ~8 m. The hilltop around the heavily instrumented white fir (CZT-1) is an area of particularly high porosity, with porosities of 0.2 extending down to about 10 m depth and 0.05 down to 15 m depth. Uncertainties in the derived fractional porosity due to potential mineralogical variability are about ±0.1 at the surface, but the uncertainty becomes much smaller with depth. We can perform two rough checks on the validity of this model. First, we note that the predicted velocity at zero porosity for this mineralogy is about 4.2 km/s, close to the 4.0 km/s observed on the granite outcrop; this suggests that our porosity model is calibrated to within ±5%, at least at the low-porosity end. Second, measurements of porosity from soil and saprolite samples acquired by hand augering show that the porosities predicted by our model are plausible.

Coupled Analysis of Refraction and Resistivity

Insight into the subsurface structure and water content of Line 5 can be gained from a detailed comparison of the resistivity model to the seismic velocity model (Figure 8). The comparison shows several significant similarities as well as differences. High resistivities (>10^4

ohm-m) reach the surface just south of the hilltop, where a bedrock outcrop occurs, consistent with the expected high resistivity of granite (~10^4 ohm-m; REF). Velocities there are nearly 2 km/s at the surface, which we interpret as rock that "rings to the hammer" but has some porosity due to minor weathering (microporosity) and/or fractures (macroporosity). Beneath the hilltop, the top of the highly resistive body matches well with the 2 km/s seismic velocity contour, consistent with this interpretation; this slightly weathered bedrock appears to have unsaturated (dry) pores and is thus electrically resistive. The underlying 4 km/s contour, which marks the transition to virtually unweathered bedrock according to the porosity model (Fig. 10) and the Line 9 results (Fig. 6), does not appear as a distinct boundary in the resistivity model. Beneath the upper hillslope (x=150-200 m), the upper ~15 m of the subsurface has velocities <2.0 km/s, corresponding to saprolite, and lower resistivity values (~10^3 ohm-m) that likely indicate clay content and/or the presence of small amounts of water.

The lowest resistivity values in the model (<100 ohm-m) exist in a northward-dipping, highly conductive body in the uppermost 5-10 m beneath the meadow (x=320-370 m). This body very likely corresponds to the water table; the meadow itself was water-logged and marshy at the surface during the survey, consistent with the low resistivity measurements (REF). Deeper pockets of low resistivity are present beneath the edges of the meadow as well, possibly indicating local saturated zones within the bedrock.

The most striking contrast between the velocity and resistivity models occurs at depths >20 m beneath the hillslope (~x=220-250 m), where a large lateral contrast in resistivity occurs with virtually no effect on the velocity contours. Over a lateral distance of only 30 m, resistivity decreases from >14,000 ohm-m to <200 ohm-m, while the 2 km/s and 4 km/s velocity contours are nearly horizontal. Barring a large change in mineralogy of the subsurface, the most likely

explanation for this change is a contrast in the saturation of pore spaces (microporosity and/or fracture porosity) in the bedrock, from dry porosity at the top of the hillslope to saturated beneath the lower hillslope and meadow. Because this contrast occurs near the base of the hillslope, we hypothesize that the contrast in saturation may be a permeability phenomenon: if the dominant direction of subsurface fluid flow is downslope, water may not have time to penetrate the low-porosity, weathered bedrock beneath the slope, but may be able to seep into bedrock cracks beneath the meadow, where hydraulic gradients will be lower.

Regolith Thickness

Our seismic velocity models enable a thorough view of the thicknesses of the saprolite and weathered bedrock in the SSCZO. For this purpose we choose the 2 and 4 km/s velocity contours and show a histogram of thicknesses from the surface to those contours in Figure 10. We interpret the 4 km/s velocity contour as the transition between regolith and largely unweathered rock; this is supported by the porosity model and the velocities of the outcrop studied on Line 9 (Figure 1C), which we take to represent more-or-less pristine granite with few fractures and joints. This implies that the 4 km/s contour marks the depth of significant subsurface weathering. We interpret the 2 km/s contour as the approximate transition from saprolite to rock that "rings to the hammer," as indicated by the velocities near the surface at the south end of Line 5; this interpretation is consistent with other seismic studies of regolith (REFS). The histogram shows that the total regolith thickness varies from 5-35 m, with an average around 25 m; saprolite thickness varies from 0-23 m, with an average around 10 m.

In addition to quantifying the overall uncertainty associated with variance in starting velocity models, our Monte Carlo analysis also permits us to quantify how variations in the

starting model affect the inferred depth of different constant velocity contours in the subsurface (Figure 4, black lines). To the extent that our sensitivity analysis of Line 5 (Figure 5) is representative of the scale of variance we would see in sensitivity analyses of the other lines, we can use it to put realistic bounds on the depth of different velocity contours in each of our other velocity models (Figure 6). This allows us to infer variations in regolith thickness along each profile (upper panels of Figures 4 and 6). Across each of our lines, regolith is remarkably thick (except on Line 9, where it is absent). On Line 5, regolith thickness ranges from ~10 to 40 m (average = XX m), with the thickest regolith on the ridge (beneath CZT-1) and the thinnest regolith at the base of the hillslope, just south of the swampy meadow. Similar variations are observed on other lines, with a general tendency toward thicker regolith at ridge crests (Fig. 6).

Weathering Timescales (NEEDS WORK!)

The seismic and resistivity data acquired here show a thick weathering zone overlying granite bedrock in the SSCZO.

It is important to point out that the velocity models presented here give an accurate view of the thickness and general properties of the saprolite and weathered bedrock, but lack the resolution to discern some important details, such as velocity gradients. For example, with traveltime analysis alone we cannot say whether velocity increases smoothly with depth through the saprolite or takes several small jumps, corresponding to sharp "fronts" in degree of weathering. Amplitude analysis (e.g., by waveform tomography) could help resolve such details.

Future work

Future work in the SSCZO should include drilling, including downhole geophysical logging and coring. Core samples would enable direct testing of our porosity and weathering models and would provide key ground truth of the physical properties imaged here. Time-lapse geophysical imaging would enable seasonal and annual changes in subsurface structure (e.g., due to changing water availability) to be discerned and linked to evapotranspiration processes.

Conclusions

Our seismic velocity and electrical resistivity models of the subsurface in the SSCZO show a surprisingly thick weathering zone, with unweathered granite lying an average of 25 m below the surface, and highly weathered saprolite extending to an average depth of 10 m. Our cosmogenic nuclide based estimates of erosion rates vary from XX to XX m/Ma across the site; hence measured regolith thicknesses correspond to a turnover times of XX,000 and XX,0000 years for the profile as a whole and for highly weathered saprolite, respectively, indicating that weathering measured from regolith at the surface integrates subsurface weathering over late Pleistocene variations in climate. Hence, to the extent that climate modulates subsurface weathering at the SSCZO, modern surface processes may be influenced to a legacy of past conditions. Porosities derived from a rock physics model of seismic velocities decrease from ~50% at the surface to zero at the base of weathered rock along one intensively studied transect. Model-predicted porosities are broadly consistent with values measured from both physical and chemical properties of saprolite and rock, suggesting that our analysis of the geophysical data provides robust first-order constraints on subsurface weathering and water storage across the SSCZO. Our results indicate that saprolite is both a crucial reservoir of water and major source

of weathering fluxes, accommodating an average of ~2 m^3/m^2 of water (and up to 5 m^3/m^2 in places) and accounting for roughly XX% of the total chemical erosion flux at the SSCZO.

	g cm^{-3}		cm^3 cm^{-3}		cm^3 cm^{-3}		cm^3 cm^{-3}	
Soil Depth (cm)	Mean ρ_b	σ	Mean φ	σ	Mean VWC	σ	Mean VAC	σ
30	1.27	0.14	0.52	0.05	0.13	0.05	0.39	0.05
60	1.43	0.18	0.46	0.07	0.11	0.01	0.35	0.01
75	1.30		0.51		0.11		0.40	
90	1.39	0.15	0.48	0.06	0.12	0.02	0.36	0.02
120	1.51	0.07	0.43	0.03	0.15	0.03	0.28	0.03
150	1.52	0.13	0.43	0.05	0.16	0.04	0.27	0.04
180	1.44	0.10	0.46	0.04	0.18	0.01	0.27	0.01
200	1.44	0.17	0.46	0.07	0.14	0.05	0.31	0.05
250	1.69		0.36		0.09		0.28	
300	1.47		0.44		0.19		0.25	
330	1.48		0.44		0.21		0.23	
390	1.27		0.52		0.15		0.37	
450	1.51		0.43		0.31		0.12	
540	1.56		0.41		0.25		0.16	

Table 1. Mean bulk density and porosity values with standard deviations for all samples taken at the specific depths for the three different locations. At depths greater than 250 cm samples had too few values or only a single value for calculation of a standard deviation (σ). VWC = Volumetric Water Content = water filled porosity; VAC = Volumetric Air Content = air-filled porosity.
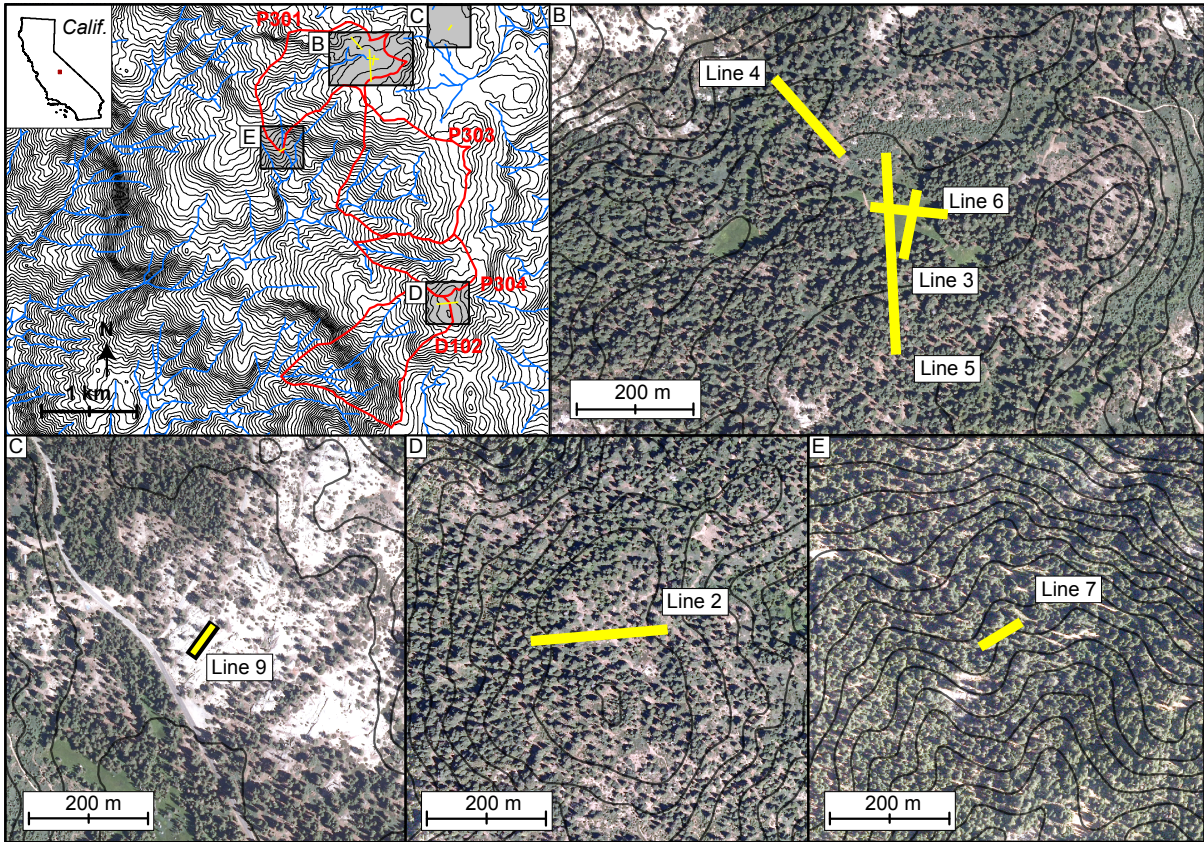
Figure 1. Location map, showing CZO catchments (A), which drain to Providence and Duff creeks in granitic terrain of the Southern Sierra Nevada. Lines 3-6 are located at the head of P301, with 3, 5 and 6 centered around a meadow heavily instrumented meadow (B). The southern end of Line 5 starts near CZT-1, a heavily instrumented white fir at the P301 drainage divide. Line 9 (C) spans an expanse of bare bedrock near Glen Meadow. Line 2 (D) spans a convex forested ridge at the head of D102 and Line 7 (E) spans the channel and adjacent slopes near a low-flow weir at the mouth of P301. Contour spacing is XX m in A and XX m in B-E.
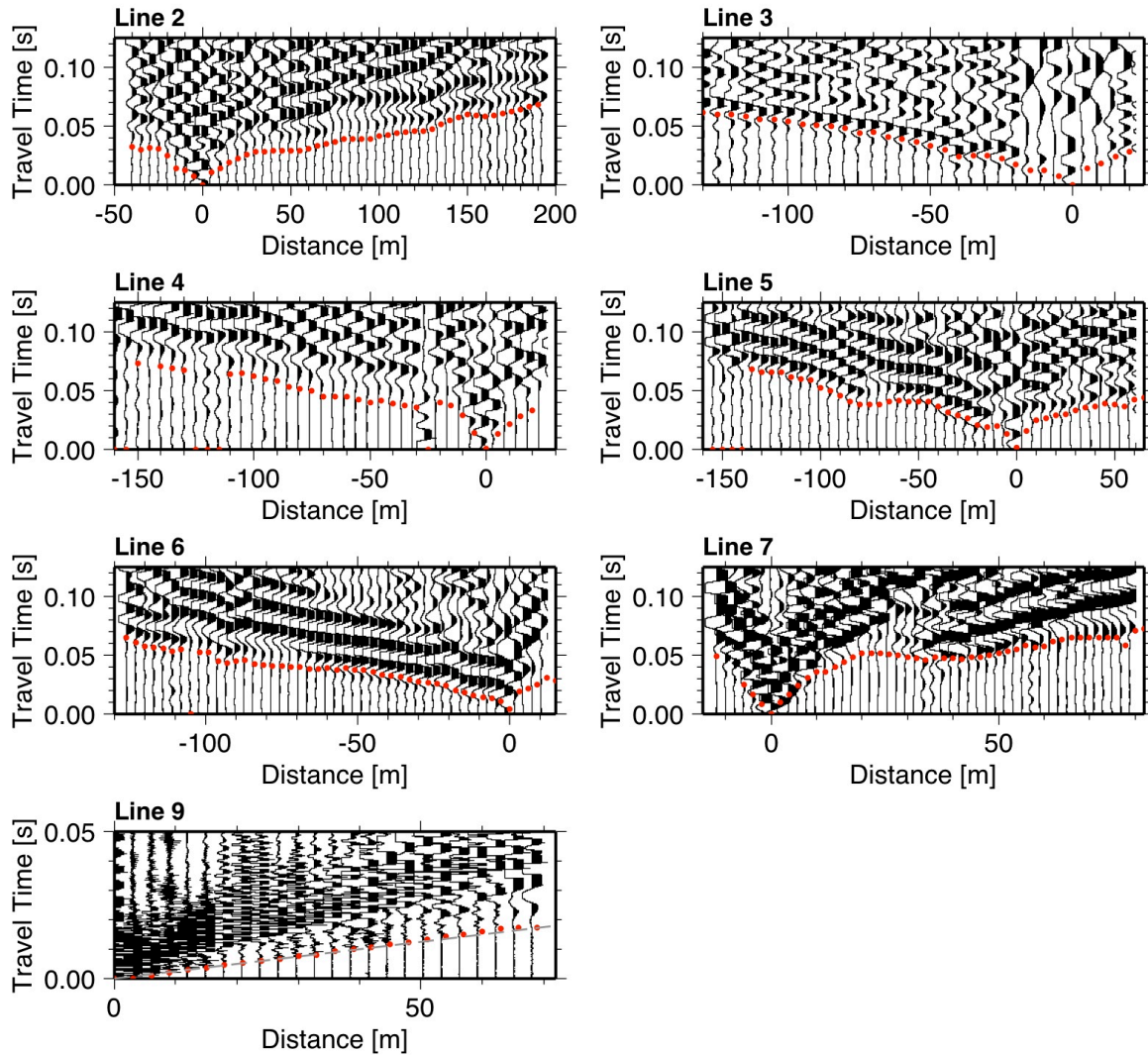
Figure 2. Seismic refraction data from geophones for one set of stacked records on each line. X axis is distance away from source (in this case a sledge hammer struck on a 400 cm² steel plate) at X = 0. Data quality is typical of stacked shots at other locations and is generally sufficient for straightforward manual picking of first arrivals (here marked by red dots on each plot). Dashed line on data from Line 9, which spans a bare bedrock ridge, has a slope of exactly 4 km/s and is consistent with manually picked first arrivals. The same strong match to a 4 km/s slope can be seen on all of the stacked records for Line 9, implying that 4 km/s at depth is representative of minimally altered and fractured granite. Scaling on the vertical axis is the same for all lines except Line 9.
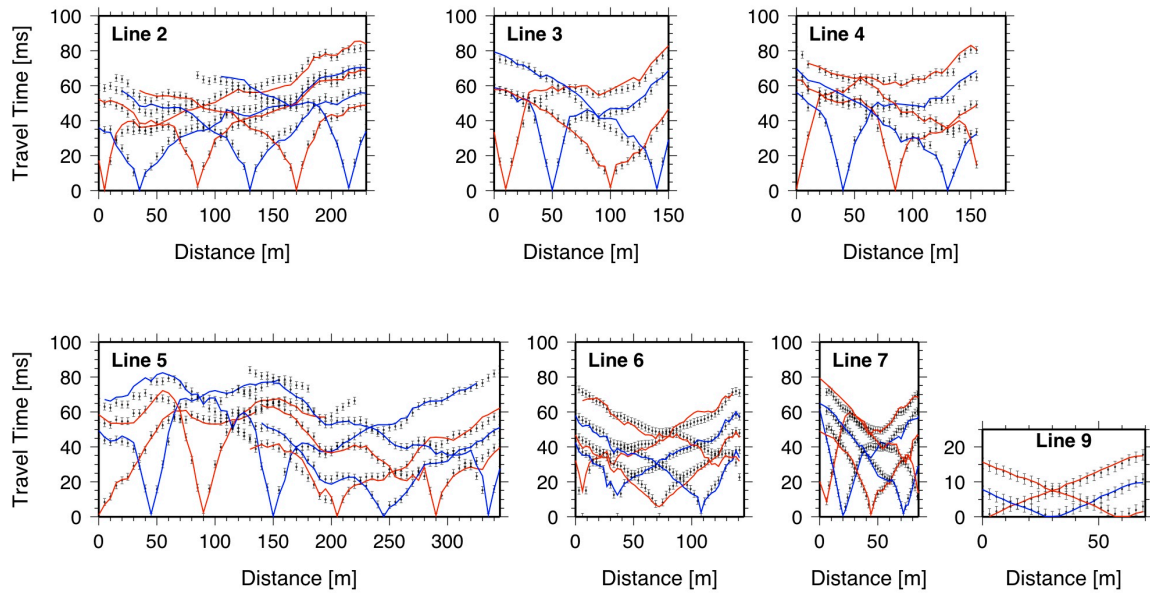
Figure 3. Travel time plots showing observed first-arrival travel times (dots with error bars) and predicted travel times from best-fit velocity models (red or blue lines). To maintain clarity, only a subset (about 20%) of the shots are plotted here. Scaling is consistent for all plots except Line 9.
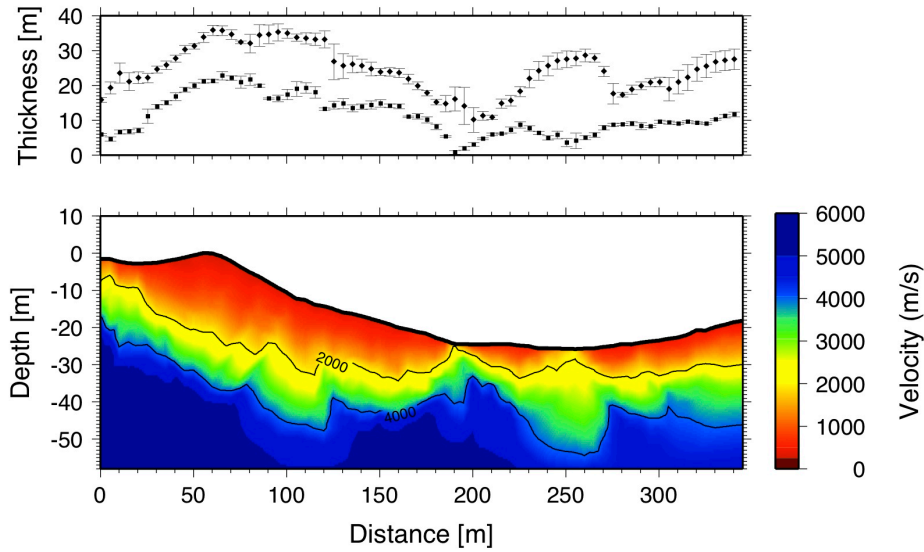
Figure 4. (Bottom) Velocity model of Line 5 from inversion of first-arrival travel times. (Top) Depth from the surface to the 2000 m/s and 4000 m/s contours. Error bars reflect variations observed in a Monte Carlo ensemble of solutions that result from a range of starting models (see text). Depth to the 4000 m/s contour varies from 10 to 35 m (average XX m) and is highest at the crest of the forested slope, under CZT-1, a heavily instrumented white fir. In contrast, under the swampy meadow, depth to the 4000 m/s contour is shallowest and most variable, ranging from ~10 to 30 m over just 60 m of horizontal distance.
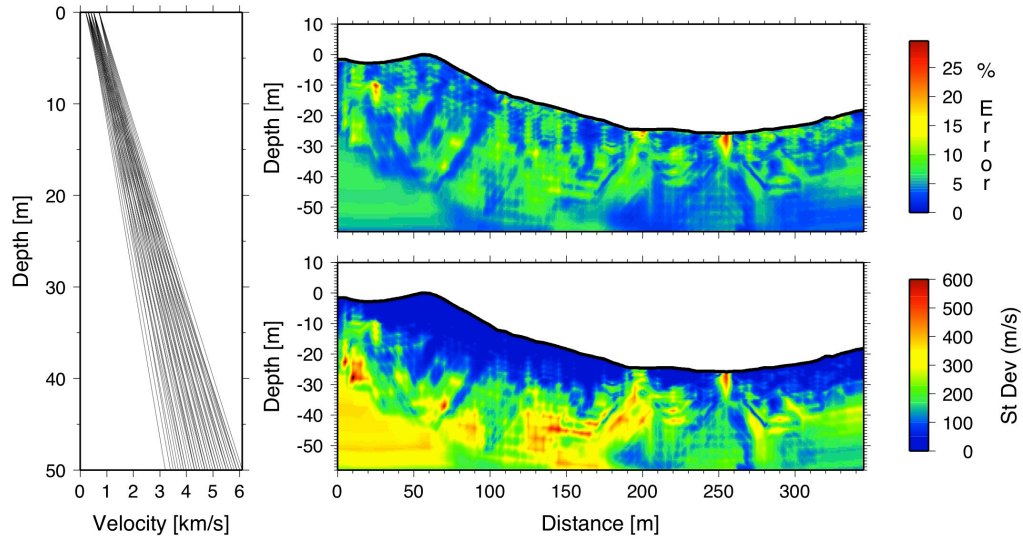
Figure 5. Results of Monte Carlo analysis of uncertainties in seismic velocity on Line 5. (Left) Velocity-depth curves (in depth below surface) of 50 starting models used to generate ensemble of inverted models. (Right) Variance among final inversion in ensemble, expressed as standard deviation (bottom) and percent error (top). Velocities in the upper 10 m are generally known to ±100 m/s or better, and ±300 m/s elsewhere.
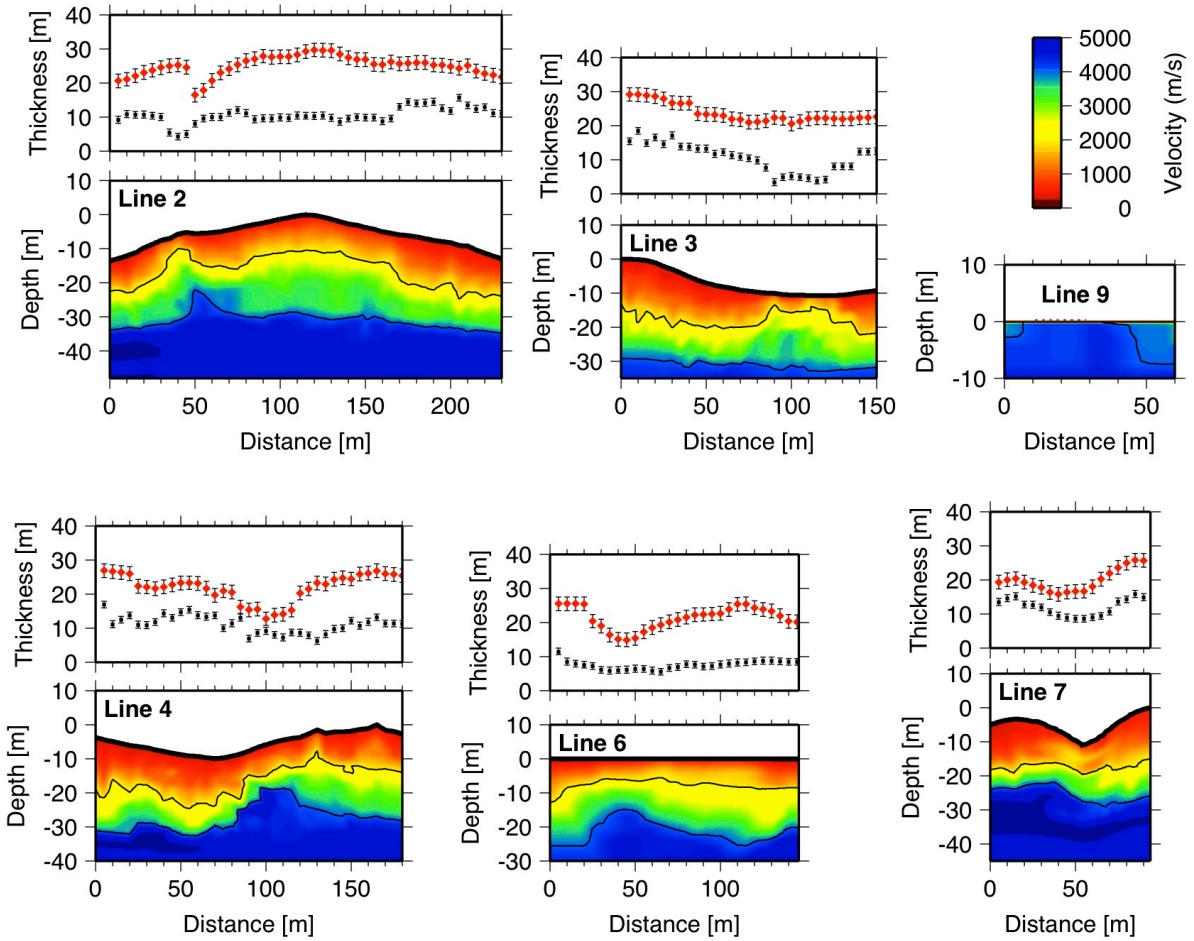
Figure 6. Velocity models from inversion of first-arrival travel times on seismic lines 2, 3, 4, 6, 7, and 9. Velocities of 4000 m/s at the surface on Line 9, acquired on an extensive granite outcrop (Fig. 1c), enable interpretation of 4000 m/s velocities (blue shades) on other lines as coherent bedrock at depth. Black circles and red diamonds represent the depth from the surface to the 2000 m/s and 4000 m/s contours, respectively. Error bars were set at ±1 m and 2 m, respectively, for the 2000 m/s and 4000 m/s contours, based on average uncertainties from Monte Carlo analysis of Line 5 (Figure 4).
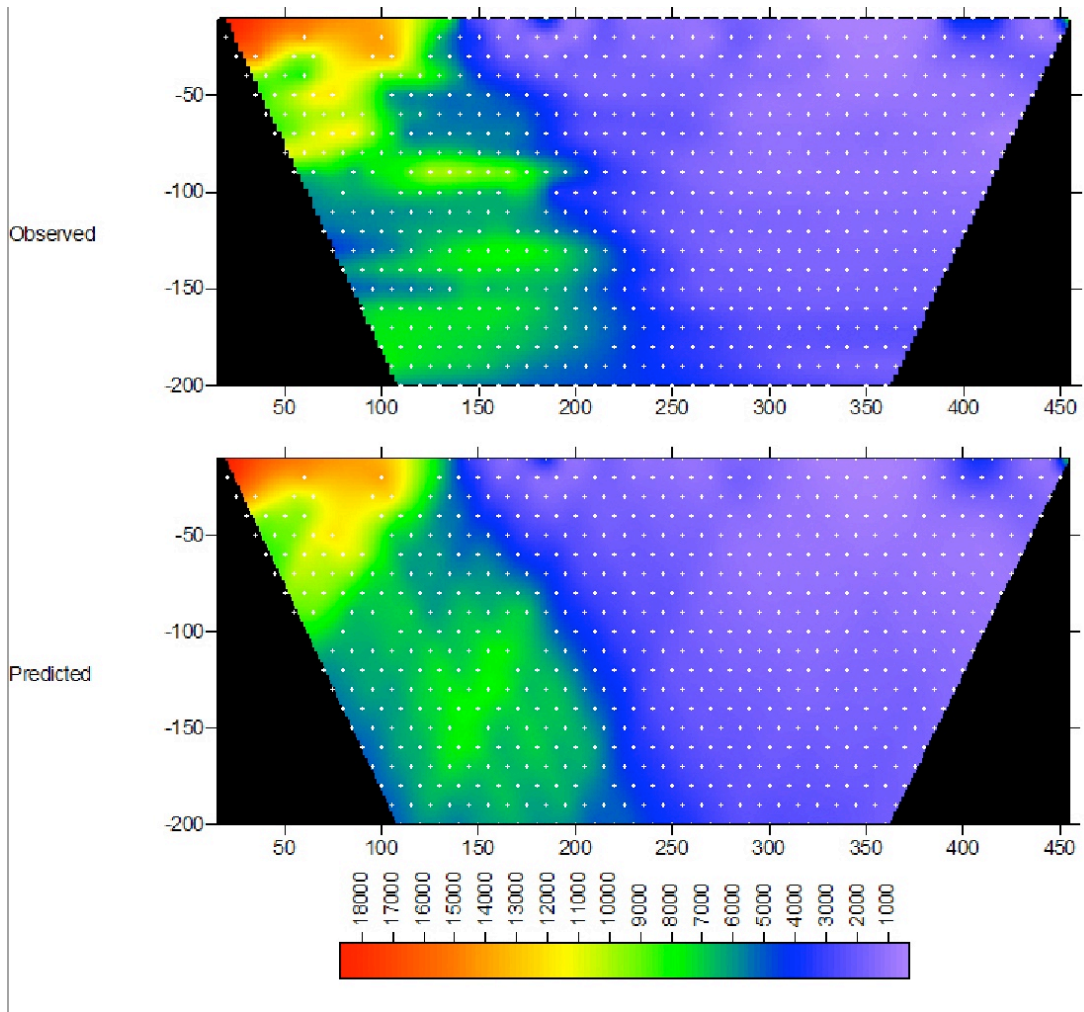
Figure 7. Pseudo-sections of observed (top) and predicted (bottom) resistivities from Line 5.
Note the strong contrast between high resistivities on the left and low resistivities on the
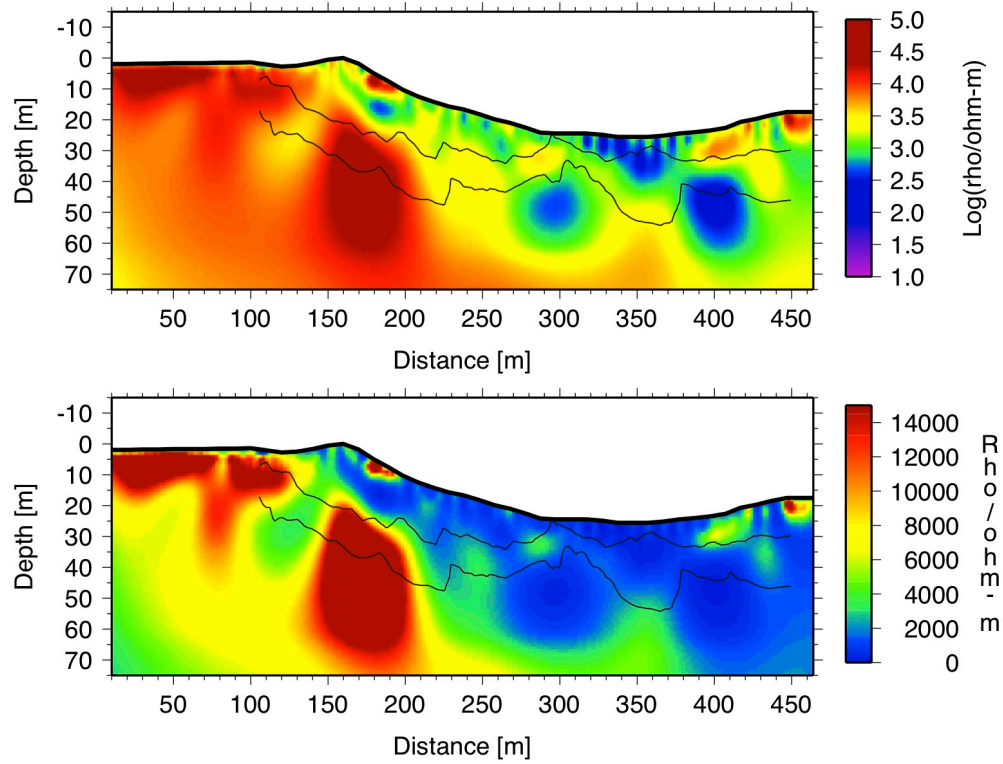right. NEED TO EXPLAIN WHAT THIS IMPLIES

Figure 8. Resistivity model on Line 5, plotted in log (top) and linear (bottom) scales. Black lines are the 2000 m/s and 4000 m/s velocity contours from the Monte-Carlo-averaged velocity model shown in Fig. 5.
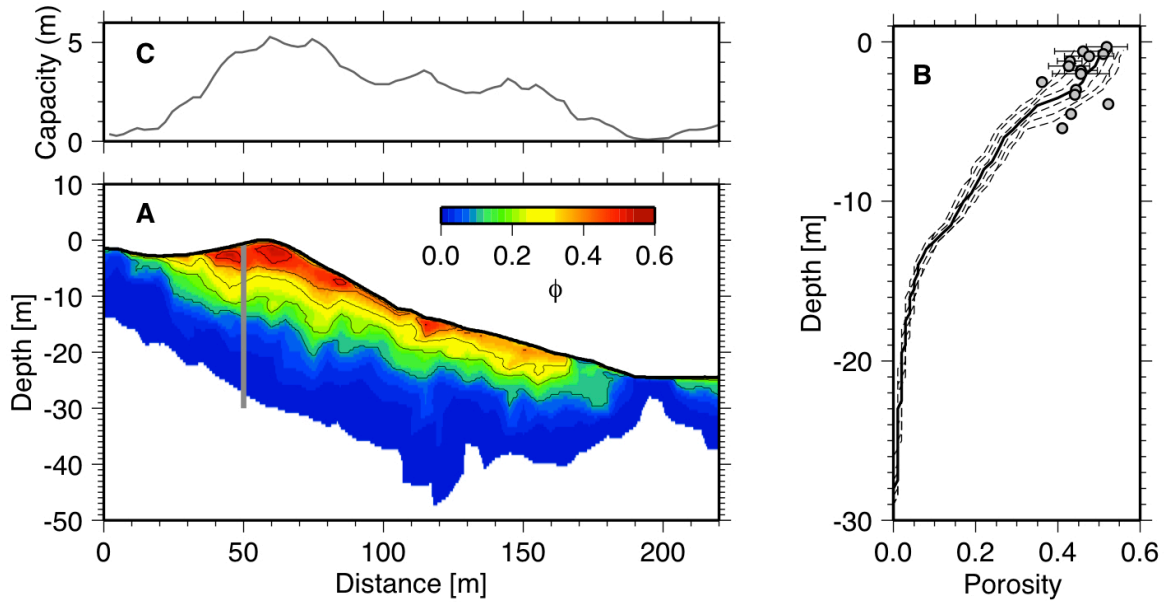
Figure 9. Line 5: (A) Porosity model on portion of Line 5, calculated from seismic velocities using a rock physics model, and assuming dry porosity and a composition of 50% feldspar, 25% quartz, and 25% clay. Porosity is contoured every 0.1 (10%). White region at base shows area where porosity is predicted to be zero (i.e., unweathered bedrock). Note that this is a minimum porosity for that composition; if pore space is saturated, higher porosities would be needed to match seismic velocities. (B) Predicted porosity-depth profiles at the location of the gray line in figure A, near the white fir CZT-1. The solid line shows the predicted porosity for the composition assumed in part A; dashed lines show sensitivity of porosity calculation to variation in composition over a range of 25-50% quartz, 10-65% feldspar, and 0-65% clay. (C) Total water storage capacity of the subsurface, in meters of water, calculated by integrating porosity profiles with depth at all positions across the model. At the top of the hill near CZT-1, the subsurface could hold ~5 meters of water if fully saturated.
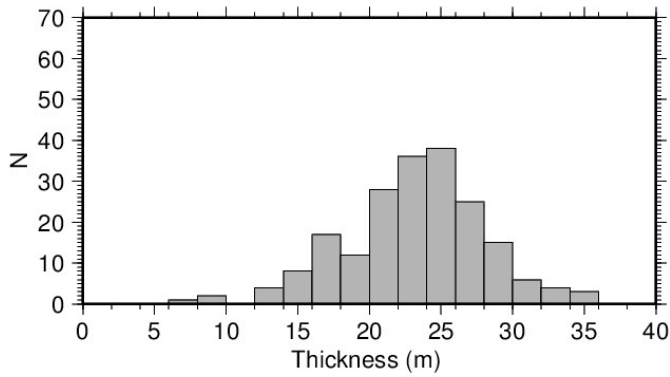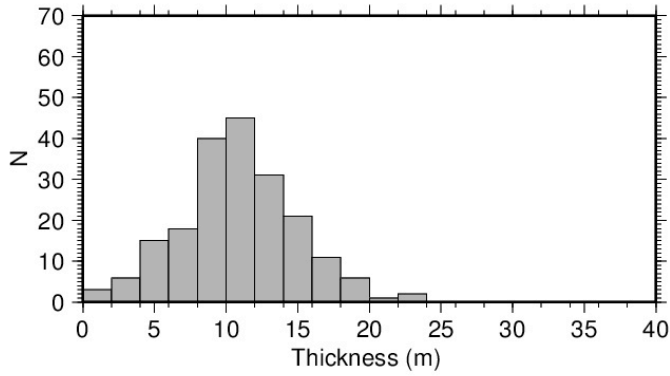
Figure 10. Histograms of thickness to 2 km/s contour (top) and to 4 km/s (bottom), compiled from all lines except Line 9. Mean thickness to 2 km/s contour, which represents relatively porous saprolite, is about 10 m; mean thickness to 4 km/s contour, which represents unweathered bedrock, is about 25 m.

———

References

Anderson, S. P., W. E. Dietrich, and G. H. Brimhall (2002), Weathering profiles, mass-balance analysis, and rates of solute loss: Linkages between weathering and erosion in a small, steep catchment, *Geological Society of America Bulletin*, *114*(9), 1143.

Brantley, S. L., and M. Lebedeva (2011), Learning to Read the Chemistry of Regolith to Understand the Critical Zone, in *Annual Review of Earth and Planetary Sciences, Vol 39*, edited by R. Jeanloz and K. H. Freeman, pp. 387-416.

Ceryan, S. (2008), New chemical weathering indices for estimating the mechanical properties of rocks: A case study from the Kurtun granodiorite, NE turkey, *Turkish Journal of Earth Sciences*, *17*(1), 187-207.

Dvorkin, J., and A. Nur (1996), Elasticity of high-porosity sandstones: Theory for two North Sea data sets, *Geophysics*, *61*(5), 1363-1370.

Helgerud, M. B., J. Dvorkin, A. Nur, A. Sakai, and T. Collett (1999), Elastic-wave velocity in marine sediments with gas hydrates: Effective medium modeling, *Geophysical Research Letters*, *26*, 2021–2024.

Hill, R. (1952), The elastic behaviour of a crystalline aggregate, *Proceedings of the Physical Society of London Section A*, *65*(389), 349-355.

Mindlin, R. D. (1949), Compliance of elastic bodies in contact, *J. Appl. Mech.-Trans. ASME*, *16*(3), 259-268.

Nur, A., G. Mavko, J. Dvorkin, and D. Galmudi (1998), Critical Porosity: A Key to Relating Physical Properties to Porosity in Rocks, *The Leading Edge*, *17*, 357-362.